Naval Research Laboratory

Washington, DC 20375-5320

NRL/MR/6794--14-9586

Pixel Dynamics Analysis of Photospheric Spectral Data

Anthony Rasca

National Research Council Postdoctoral Associate
Beam Physics Branch
Plasma Physics Division

James Chen

Beam Physics Branch
Plasma Physics Division

November 13, 2014

REPORT DOCUMENTATION PAGE

Form Approved
OMB No. 0704-0188

1. REPORT DATE *(DD-MM-YYYY)*	**2. REPORT TYPE**	**3. DATES COVERED** *(From - To)*
13-11-2014	Interim	March 2014 – August 2014

4. TITLE AND SUBTITLE

Pixel Dynamics Analysis of Photospheric Spectral Data

5a. CONTRACT NUMBER

5b. GRANT NUMBER

5c. PROGRAM ELEMENT NUMBER

6. AUTHOR(S)

Anthony Rasca* and James Chen

5d. PROJECT NUMBER
67-4989-04

5e. TASK NUMBER

5f. WORK UNIT NUMBER

7. PERFORMING ORGANIZATION NAME(S) AND ADDRESS(ES)

Naval Research Laboratory
4555 Overlook Avenue, SW
Washington, DC 20375-5320

8. PERFORMING ORGANIZATION REPORT NUMBER

NRL/MR/6794--14-9586

9. SPONSORING / MONITORING AGENCY NAME(S) AND ADDRESS(ES)

Naval Research Laboratory
4555 Overlook Avenue, SW
Washington, DC 20375-5320

10. SPONSOR / MONITOR'S ACRONYM(S)

NRL

11. SPONSOR / MONITOR'S REPORT NUMBER(S)

12. DISTRIBUTION / AVAILABILITY STATEMENT

Approved for public release; distribution is unlimited.

13. SUPPLEMENTARY NOTES

*National Research Council Postdoctoral Associate

14. ABSTRACT

A new method has been developed to analyze high-resolution spectral data of the solar photosphere and chromosphere. The data format is a two-dimensional (2-D) time-series of images. The method uses emission or absorption lines in the intensity and polarization data (Stokes parameters). Each pixel contains quantitative information on the spectral profiles of selected lines, such as the line width, degree of asymmetry, and "peakedness." The 2-D time-series is first averaged in time pixel-by-pixel. A derivative time-series is constructed such that each image in the time-series is characterized by the pixel-by-pixel deviations from the average. The pixel fluctuation distribution (PFD) function is constructed and its statistical properties are calculated. Such properties including the mean, variance, skewness, and kurtosis are computed as functions of time and are used to precisely quantify temporal variations in the observed spectral data. In this work, the method is applied to photospheric absorption lines (Fe I 6301.5 Å and 6302.5 Å) from quiet-Sun regions and active regions on the solar photosphere, obtained by the vector spectromagnetograph (VSM) of the Synoptic Optical Long-term Investigations of the Sun (SOLIS) of the National Solar Observatory (NSO).

15. SUBJECT TERMS

Spectroheliograph data
Photospheric and chromospheric spectral data
Vector magnetogram
Statistical analysis
Skewness
Kurtosis

16. SECURITY CLASSIFICATION OF:			**17. LIMITATION OF ABSTRACT**	**18. NUMBER OF PAGES**	**19a. NAME OF RESPONSIBLE PERSON**
a. REPORT	**b. ABSTRACT**	**c. THIS PAGE**			James Chen
Unclassified Unlimited	Unclassified Unlimited	Unclassified Unlimited	Unclassified Unlimited	25	**19b. TELEPHONE NUMBER** *(include area code)* (202) 767-3134

Standard Form 298 (Rev. 8-98)
Prescribed by ANSI Std. Z39.18

Pixel Dynamics Analysis of Photospheric Spectral Data

Anthony Rasca[1,2] and James Chen[2]

1. National Research Council Postdoctoral Associate

2. Plasma Physics Division, Naval Research Laboratory, Washington, DC 20375

James.Chen@nrl.navy.mil

ABSTRACT

A new method has been developed to analyze high-resolution spectral data of the solar photosphere and chromosphere. The data format is a two-dimensional (2-D) time-series of images. The method uses emission or absorption lines in the intensity and polarization data (Stokes parameters). Each pixel contains quantitative information on the spectral profiles of selected lines, such as the line width, degree of asymmetry, and "peakedness." The 2-D time-series is first averaged in time pixel-by-pixel. A derivative time-series is constructed such that each image in the time-series is characterized by the pixel-by-pixel deviations from the average. The pixel fluctuation distribution (PFD) function is constructed and its statistical properties are calculated. Such properties including the mean, variance, skewness, and kurtosis are computed as functions of time and are used to precisely quantify temporal variations in the observed spectral data. In this work, the method is applied to photospheric absorption lines (Fe I 6301.5 Å and 6302.5 Å) from quiet-Sun regions and active regions on the solar photosphere, obtained by the vector spectromagnetograph (VSM) of the Synoptic Optical Long-term Investigations of the Sun (SOLIS) of the National Solar Observatory (NSO).

Manuscript approved October 10, 2014

1. Introduction

The solar photosphere (light sphere) is the innermost layer of the solar atmosphere that is directly observable by remote sensing methods. Below the photosphere, photons are collisionally coupled to the plasmas at all wavelengths whereas the hot, fully ionized corona—the atmosphere above the photosphere—is optically thin to a wide range of photon wavelengths. The photosphere is the optical boundary layer where the atmosphere makes the transition from an optically thick to an optically thin state. Numerous energetic plasma phenomena in the corona have been observed. The most energetic of them—solar eruptions—are driven by magnetic energy in the form of magnetic force (Lorentz force) converting magnetic energy into kinetic energy, and induced electric fields accelerate particles resulting in electromagnetic radiation. Solar eruptions are observed as coronal mass ejections (CMEs), eruptive prominences (EPs), and solar flares, depending on the observing methods and wavelengths used. Eruptions are sporadic and dramatic in appearance. As a result, they have attracted much scientific attention since the first observation of flares in 1859 (Carrington 1860; Hodgson 1860). A typical eruptive event releases an estimated 10^{32}–10^{33} erg of energy in several hours. The most dominant of solar energy, of course, is in the form of the "white light" at the effective (black-body radiation) temperature $T_s \simeq$5800 K, with the total luminosity $\mathcal{L}_\odot = 3.8\times10^{33}$ erg s^{-1}. Here, subscript "s" refers to the photospheric "surface." In sunspots, which appear as black spots in white-light images, the temperature is lower at $T_s \simeq 4500$ K.

All energy manifested by the Sun is ultimately generated in the core by nuclear fusion and eventually passes through the photosphere. The photosphere exhibits the ubiquitous granular motion corresponding to the convection flows turning over at the surface. This is where the plasma radiatively cools, releasing the photons into the optically thin corona. In 1908, Hale discovered Zeeman splitting in the photon spectra from sunspots (Hale, 1908), demonstrating the existence of solar magnetism. Since then, solar magnetic fields have been extensively observed by remote sensing using the Zeeman effect. In particular, the circular polarization in photons emitted along the surface magnetic field—the line-of-sight (LOS) component of the surface magnetic field—has been routinely measured using magnetographs, which measure the spectral properties including polarization. Such magnetogram data provide polarity and intensity maps of the resolved LOS magnetic field component in the solar disk (2-D projection of the hemispheric photospheric surface). Sunspots are found in active regions (ARs) characterized by concentrations of strongly magnetized features. Figure 1 shows a magnetogram obtained by the Michelson Doppler Imager (MDI, Scherrer et al., 1995) on the Solar and Heliospheric Observatory (SOHO) satellite (Domingo et al., 1995). In this image, white pixels show the LOS field in the positive direction (out of the surface, toward the observer), and black pixels show fields in the negative direction (into the surface, away from the observer). The strength of the observed component is shown on a grey scale.

In time-resolved magnetograms, an AR is first seen as the appearance of a pair of opposite polarity features, which correspond to sunspots in white-light images. They are presumed to be surface manifestation (a cut at the photospheric surface) of a flux rope rising from below the photosphere (Babcock 1961; Zirin 1988), and observable signatures of such "flux emergence" events have been simulated, showing the appearance of small-scale bipolar magnetic features in the photosphere (e.g., Cheung et al. 2010; Stein and Nordlund, 2012) consistent with observations (Strous et al. 1996; Strous and Zwaan, 1999). The magnetic field in the Sun is thought to be produced by the solar dynamo at the base of the convection zone.

Figure 2 schematically illustrates a "pixel" on the solar surface (viewed from above) containing unresolved magnetic loops, each of which is a flux rope of small but finite dimension. The thick arrowed lines represent such field structures above the surface. Two vertical lines representing oppositely directed field structures are shown. The sense of Zeeman-induced circular polarization (the σ^+ state) in photons propagating toward the observer is indicated, showing that the circular polarization from these magnetic elements would be canceled and that these magnetic elements are therefore undetected. The motion of the small magnetic structures may also be difficult to measure using the Doppler shift because the motion of plasma along such magnetic features and the flux of magnetic energy through the surface are not coupled. This is indicated by two short arrows (up and down) representing fluid velocity components $V_\parallel$.

The above figure shows that if a pixel contains unresolved oppositely directed magnetic fields, the actual quantity obtained from magnetograms is the net uncanceled LOS magnetic flux integrated over a pixel, $\Phi_\parallel \equiv \oint \mathbf{B} \cdot d\mathbf{a}_\perp$ where $d\mathbf{a}_\perp$ is an element of the pixel that is projected onto an imaginary plane perpendicular to the LOS. The magnetic field "magnitude" quoted in the literature is the net flux per unit area (i.e., LOS flux density), $B_\parallel = \Phi_\parallel / A_p$, where $A_p \equiv \oint da_\perp$ is the projected area corresponding to the pixel. The actual magnetic flux may be much more concentrated in unresolved magnetic "tube" or more generally in "flux ropes," in which the field is much stronger than the average flux density. The fraction of the volume occupied by the magnetized flux rope in an unresolved volume is referred to as the "filling factor." The filling factor in the photosphere is not well-established, and there is evidence that the current highest-resolution magnetograms still do not adequately resolve the surface magnetic field at least in quiet-Sun regions (Pietarila Graham et al. 2009).

The photosphere shows ubiquitous motion, resulting from the continual upwelling of magnetized plasmas from the base of the convection zone on a range of scales. Describing the dynamical system in terms of macroscopic fluid parameters, i.e., magnetohydrodynamics (MHD), the velocities of the magnetized photospheric plasmas scale with the magnetosonic

speed, with the actual speed determined by the local force imbalance (Chen 2001). Thus, all spatially localized energetic processes such as flux emergence are expected to exhibit similar velocities. Various "unusual" changes in plasma flow and magnetic field patterns in time series of images have been examined, and some types of changes have been statistically related to pre-eruptive periods. Given the above limitations in ascertaining magnetic field dynamics in the photosphere due to the unknown filling factor, we develop a method that extracts information on the sub-pixel plasma dynamics, which can complement any measurements of magnetic field and plasma dynamics. This method uses the time variations in the spectral properties accessible by remote sensing methods and enables one to quantify the temporal variations in specific spectral properties in a given solar region. Specifically, the method examines the fluctuations in the pixels of measured spectroheliographic images and accurately determines the time variation of the statistical properties of the pixel fluctuation distribution (PFD) functions. The method also allows one to identify the pixels that are responsible for the observed changes so that one can determine the morphological changes and their temporal profiles.

The basic algorithm was previously developed for analyzing time series of intensity images in which each pixel contains one intensity value (Schuck et al., 2004). The present work extends the algorithm to spectrographic images so that the information for each pixel is a set of resolved spectral functions. The method can be used to extract sub-grid information on unresolved plasma properties as well as magnetic field dynamics.

2. Input Data Time Series

Consider a specified region $\mathcal{R}$ observed with N pixels. Let there be M images in the two dimensional (2D) time series. Let the n-th pixel of the m-th image be characterized by a set of spectral profiles, $S_m(\lambda|n)$, where $S = I, Q, U, V$ refers to intensity profile for different Stokes parameters, $m = 1, \ldots, M$ is the image counter, $n = 1, \ldots, N$ is the pixel counter within an image, and λ is the wavelength. Here, the image counter m starts with $m = 1$ at the first observing time $t = 0$.

2.1. Pixel Characteristics

The objective of the work is to quantify variations in specific spectral line profiles. Figure 3 shows a plot of the photospheric spectrum measured by the Vector Spectromagnetograph (VSM) of the Synoptic Optical Long-term Investigations of the Sun (SOLIS) facility

of the National Solar Observatory (NSO) (Balasubramaniam and Pevtsov 2011). The plot contains Fe I absorption lines centered at 6301.5 Å and 6302.5 Å. The two smaller absorption lines are telluric lines.

The analysis is carried out for a range of wavelengths about a known emission or absorption line centered at, say, λ_c, and the profile $S_m(\lambda|n)$ of interest is understood to be defined for $[\lambda_c - \Delta\lambda, \lambda_c + \Delta\lambda]$ for some suitably chosen $\Delta\lambda$. In this wavelength range, the spectrum is resolved into K evenly spaced intervals and $K+1$ spectral points, λ_k, where $k = 1, \ldots, K+1$ with $\lambda_1 \equiv \lambda_c - \Delta\lambda$ and $\lambda_{K+1} \equiv \lambda_c + \Delta\lambda$.. Thus, the measured photon data have the form $S_m(\lambda_k|n)$. In practice, an absorption line profile, which is a depression in the observed intensity curve, is converted to a peak in order to determine the line profile properties. Thus, we define the line profile function for the n-th pixel of the m-th image

$$\mathcal{S}_m(\lambda_k|n) \equiv |S_m(\lambda_k|n) - S_{m0}|, \tag{1}$$

where $S = I$, Q, U, or V, and S_{m0} is the suitably chosen "background" intensity level. For $S = Q$, for example, we write $\mathcal{Q}_m(\lambda_k|n) = |Q_m(\lambda_k|n) - Q_{m0}|$ and similarly for the total intensity $S = I$, we have $\mathcal{I}_m(\lambda_k|n) = |I_m(\lambda_k|n) - I_{m0}|$. We then define the normalized line profile function

$$\hat{\mathcal{S}}_m(\lambda_k|n) \equiv \frac{1}{\mathcal{N}_m}\mathcal{S}_m(\lambda_k|n) \tag{2}$$

such that

$$\sum_{k=1}^{K+1} \hat{\mathcal{S}}_m(\lambda_k|n) = 1, \tag{3}$$

where $\mathcal{N}_m = \sum_{k=1}^{K+1} \mathcal{S}_m(\lambda_k|n)$. In effect, this function is a statistical distribution function for the variable λ_k in the range $[\lambda_1, \lambda_{K+1}]$ for the n-th pixel in the m-th image frame.

Spectral lines from a volume of plasma at one temperature generally have the so-called Voigt profile, which is the convolution of a Gaussian and a Lorentzian. It is symmetric and appears similar to a Gaussian with flatter tails. If the unresolved plasma elements emitting the detected photons are not uniform within a pixel, the line profile in the pixel can deviate from this profile. As the first step, we calculate a number of spectral line characteristics for each pixel. For the n-th pixel of the m-th image in the time series for the Stokes parameter S, the center of the observed spectral line where the intensity is minimum (maximum) for an absorption (emission) line is at

$$\langle\lambda_m^S\rangle(n) = \frac{1}{K+1}\sum_{k=1}^{K+1} \lambda_k \hat{\mathcal{S}}_m(\lambda_k|n). \tag{4}$$

This may be shifted from the known spectral line center at λ_c. This is defined by

$$\mathcal{D}_m^S(n) = \lambda_c - \langle\lambda_m^S\rangle(n). \tag{5}$$

The line width is given by

$$\delta\lambda_m^S(n) = \left[\frac{1}{K}\sum_{k=1}^{K+1}[\lambda_k - \langle\lambda_m^S\rangle(n)]^2\hat{\mathcal{S}}_m(\lambda_k|n)\right]^{1/2}. \tag{6}$$

The degree of asymmetry of the line is defined by the dimensionless quantity

$$\mathcal{A}_m^S(n) = \frac{1}{(K+1)(\delta\lambda_m^S)^3}\sum_{k=1}^{K+1}[\lambda_k - \langle\lambda_m^S\rangle(n)]^3\hat{\mathcal{S}}_m(\lambda_k|n) \tag{7}$$

and the flatness of the tail is given by the dimensionless measure

$$\mathcal{F}_m^S(n) = \frac{1}{(K+1)(\delta\lambda_m^S)^4}\sum_{k=1}^{K+1}[\lambda_k - \langle\lambda_m^S\rangle(n)]^4\hat{\mathcal{S}}_m(\lambda_k|n). \tag{8}$$

If the line profile is a Gaussian, we have $\mathcal{F}_m^S(n) = 3$. For a Voigt profile, we have $\mathcal{F}_m^S(n) \neq 3$, with $\mathcal{F}_m^S(n) > 3$ (< 3) being more (less) peaked than a Gaussian. In the subsequent discussion, the superscript S denoting the Stokes parameters will be omitted for simplifying the notation, except that the actual data $\mathcal{S}_m(\lambda_k|n)$ will retain S as a reminder of the dependence on S for all of these quantities. Thus, we will use $\langle\lambda_m\rangle(n)$, $\langle\mathcal{D}_m\rangle(n)$, $\langle\delta\lambda_m\rangle(n)$, $\langle\mathcal{A}_m\rangle(n)$, and $\langle\mathcal{F}_m\rangle(n)$ to characterize each pixel with the superscript S implied in the symbols. The time-progression in these quantities is given by m.

Physically, if $\mathcal{D}_m^S(n) \neq 0$, the plasma in the pixel has an average bulk speed, with $\mathcal{D} > 0$ ($\mathcal{D} < 0$) corresponding Doppler blueshift (redshift) integrated over the pixel. Variations in the line width $\delta\lambda_m$ may indicate variations in temperature or changes in counterstreaming flows along the LOS on various scales, often referred to as "non-thermal" or "turbulent" broadening. Changes in the symmetry of the line profile $\mathcal{S}_m$, of course, connote changes in the flows along the LOS toward and away from the observer. To interpret changes in the tail flatness $\mathcal{F}_m$, we have to keep in mind that the core of an absorption line corresponds to lower heights (deeper) in the photosphere than for the tails. This effect is strongest in $\mathcal{F}_m$ but does enter into other quantities.

2.2. Pixel Fluctuation Functions

Note that the characteristic pixel quantities have the form $\mathcal{X}_m^S(n)$ where m corresponds to time. We first average the pixel quantities in time through the entire time series:

$$\langle\mathcal{X}^S\rangle(n) \equiv \frac{1}{M}\sum_{m=1}^{M}\mathcal{X}_m^S(n), \tag{9}$$

where $\mathcal{X}_m^S(n)$ denotes $\mathcal{D}_m^S(n), \delta\lambda_m^S(n), \mathcal{S}_m^S(n)$, or $\mathcal{F}_m^S(n)$. Again, the superscript S may be omitted except to specifically denote a Stokes parameter. Thus, we will use $\langle\mathcal{X}^S\rangle(n)$ and $\langle\mathcal{X}\rangle(n)$ interchangeably: $\langle\mathcal{X}\rangle(n) = \langle\mathcal{D}\rangle(n), \langle\delta\lambda\rangle(n), \langle\mathcal{S}\rangle(n), \langle\mathcal{F}\rangle(n)$. For $S = Q$, for example, this stands for $\langle\mathcal{X}\rangle(n) = \langle\mathcal{X}^Q\rangle(n) = \langle\mathcal{D}^Q\rangle(n), \langle\delta\lambda^Q\rangle(n), \langle\mathcal{S}^Q\rangle(n), \langle\mathcal{F}^Q\rangle(n)$.

We define fluctuations in the n-th pixel in the m-th image frame by

$$\delta\mathcal{X}_m(n) = \mathcal{X}_m(n) - \langle\mathcal{X}\rangle(n). \tag{10}$$

The spatial average of the pixel fluctuations in the m-th image is

$$\langle\delta\mathcal{X}_m\rangle = \frac{1}{N}\sum_{n=1}^{N}\delta\mathcal{X}_m(n). \tag{11}$$

Thus, each pixel in an image in the time series is characterized by the deviation from the time average of the spectral property in the pixel, $\delta\mathcal{X}_m(n)$, and each image is characterized by the average of the pixel fluctuation over all the pixels in the image, $\langle\delta\mathcal{X}_m\rangle$. This is the spatial average over the m-th image.

2.3. Statistics of Pixel Fluctuation

For each Stokes parameter in the m-th image, one can now define a PFD function for each pixel quantity $\mathcal{X}$, $P_m(\delta\mathcal{X})$, which is the number of pixels in the image frame m with the fluctuation value $\delta\mathcal{X} \pm \epsilon/2$, where ϵ is a suitably defined of range of $\delta\mathcal{X}$. Each image is characterized by a PFD function. A number of statistical properties of these spectral quantities can be defined. The variance σ_m^2 of the pixel fluctuations in the m-th frame is

$$\sigma_m^2 = \frac{1}{N-1}\sum_{n=1}^{N}[\delta\mathcal{X}_m(n) - \langle\delta\mathcal{Q}_m\rangle]^2, \tag{12}$$

where σ_m is the standard deviation.

The shape of the pixel PFD can be quantified by the skewness, which measures the deviation from a symmetric distribution,

$$\gamma_1(m) = \frac{1}{N\sigma_m^3}\sum_{n=1}^{N}[\delta\mathcal{X}_m(n) - \langle\delta\mathcal{X}_m\rangle]^3. \tag{13}$$

The "peakedness" or tail "flatness" can be measured by the kurtosis of the PFD defined by

$$\gamma_2(m) = \frac{1}{N\sigma_m^4}\sum_{n=1}^{N}[\delta\mathcal{X}_m(n) - \langle\delta\mathcal{X}_m\rangle]^3 - 3. \tag{14}$$

As the image frame index m increases, these statistical quantities show the time-variation of the average pixel fluctuation in the spatial region $\mathcal{R}$ at the temporal resolution of the observation.

For a symmetric distribution ($\gamma_1 = 0$), kurtosis is zero if the distribution is an exact Gaussian. If the distribution is more (less) peaked relative to a Gaussian with the same variance, the kurtosis is $\gamma_2 > 0$ ($\gamma_2 < 0$). The above definition of kurtosis is sometimes called "excess kurtosis," indicating that it measures deviations from the exact Gaussian distribution.

2.4. Measurement Uncertainties

If a photospheric or chromospheric region of interest is observed for a period of time, it moves with the surface layer of the Sun. If plasma dynamics in the region are examined, the region needs to be tracked so that the same region on the actual surface is analyzed during the period of interest. The surface, however, does not rigidly rotate, the ubiquitous granular motion can move small features in and out of the region. In addition, data from ground-based observations contain seeing effects, which are essentially random. It is important to determine the pixel fluctuations attributable to such effects in the data analysis results.

Consider a rectangular region defined by $L \times sL$ pixels, where s is the aspect ratio of the rectangle. Its area is sL^2. If a h-pixel wide band along the boundary of the rectangle is affected by surface motion of features in and out of the rectangle and seeing effects, the fraction f of the total pixels suffering such uncertainty from image to image is

$$f = \frac{2h(1+s)}{sL} \propto \frac{1}{L}. \tag{15}$$

Thus, the uncertainties arising from the fact that the actual plasma elements can cross pixel boundaries can be estimated by $f \sim 1/L$. Note that if the resolution is suffuciently fine, fluctuations due to the atmospheric seeing effects may go beyond the h-pixel wide bad and should be separately considered. Perhaps the best way to estimate the characteristic pixel fluctuation level in given region is to calculate the average fluctuation level for several different size subregions.

3. An Analysis of Photospheric Spectral Data

Figure 4 shows an area scan of the solar photosphere. The white circle indicates the circular limb of the solar disk. This scan is obtained by the SOLIS VSM instrument and

consists of 200 scan lines. The figure is an intensity map of the Stokes I data (total intensity) with red showing the highest intensity and green the lowest. The lower intensity on and near the limb is due to the so-called limb darkening effect, an artifact inherent in observing the hemispherical optically thick solar surface layer. The small light green areas marked $A1$ and $A2$ correspond to an active region containing sunspots. We have applied the pixel dynamics analysis method described above to four areas. Two are in a quiet-Sun region (containing no sunspots or other features typically associated with active regions) marked $Q1$ and $Q2$. Regions $A1$ and $A2$ contain an active region. Regions $A1$ and $Q1$ are both 100×100 square boxes while $A2$ and $Q2$ are 50×50 boxes. We will examine differences between quiet-Sun and active regions and the temporal evolution of such differences.

For each pixel region described above, and using $K = 14$ for each absorption line, we constructed PFDs for spatially averaged $\langle \mathcal{D}_m \rangle$ (red/blue shift), intensity drop, $\langle \mathcal{A}_m \rangle$ (asymmetry), and $\langle \mathcal{F}_m \rangle$ (tail flatness) of both the Fe I 6301.5 Å and Fe I 6302.5 Å absorption lines.[1] Figure 5 shows an example of a PFD for the Fe I 6301.5 Å absorption line asymmetry (region $A1$) at $t = 0.0$, 22.5, 31.5, and 42.8 minutes. The time-evolving distribution skewness is evident in these four panels. When analyzing all PFDs, the active and quiet-Sun regions are found to be primarily characterized by the variance and skewness of their absorption line redshift/blueshift and asymmetry PFDs, as well as by the spatial average for each region. These three time-varying statistical measures for the redshift and asymmetry PFDs are plotted in Figure 6. Regions $A1$ and $A2$ appear to be statistically similar, though more prominently by their redshift PFDs. The same is true for $Q1$ and $Q2$.

Unlike with active and quiet-Sun comparisons, pixel sample size is characterized by statistical differences between absorption line intensity drop and tail flatness. Figure 7 shows the time-evolving statistical measures for both the intensity drop and tail flatness PFDs. Here, $A1$ and $Q1$ are statistically similar, as well as $A2$ and $Q2$. Both absorption line property PFDs also evolve roughly proportional to each other (or inversely proportional for PFD variance), indicating a relationship between the two not observed by the PFDs in Figure 6.

4. Pixel Statistics for Eruptive Regions

Figure 6 and Figure 7 represent our initial results that have thus far been used to characterize active and quiet-Sun regions, as well as region sample size. For a secondary

[1]Results for both absorption lines are qualitatively the same, so we only present results for the Fe I 6301.5 Å absorption line

analysis, we obtained two additional SOLIS VSM data sets, from Nov. 3, 2011 and Mar. 13, 2012. Both sets of scans span ~ 1 hour and correspond to days when solar eruptions were observed on the Earth-facing side. Scans for the Nov. 3 event are composed of 201 scan lines and have a cadence of ~ 3.5 minutes per scan, while scans for the Mar. 13 event were taken with a ~ 3.2 minutes per scan cadence and consist of 251 scan lines.

These two new sets of SOLIS VSM data also revealed more inconsistent instrument movements between scans, forcing us to revise our alignment method from the previous section. In all cases, we will keep our pixel boxes fixed on the active regions of interest. With this in mind we now align our images such that the AR is in a fixed image location throughout the time sequence. This allows us to fix our pixel boxes, as opposed to shifting them to the right with each image like in the previous section. This method looks for the lowest total intensity value in the vicinity of the AR for each image and fixes each of those points to the same coordinate. Further updates will be necessary, as it does not currently account for the least intense pixel in the AR drifting from image to image.

Figure 8 shows limb-corrected intensity maps for the new SOLIS VSM area scans ($t = 0$), which have the large and small pixel boxes fixed on the ARs near the limbs, and control pixel boxes placed on the opposite ends. The same method for constructing PFDs is performed for each pixel box in Figure 8 and for each spectral absorption line property. The statistical properties of each Fe I 6301.5 Å PFD are shown in Figures 9-10 for the Nov. 3 flare event and in Figures 11-12 for the Mar. 13 flare event.

Like with the Section 3 results, global changes appear when calculating spatial averages. Many of the other PFD properties exhibit significant noise and variation, which may be attributed to imperfections with the current alignment method. This issue highlights the importance of performing further work on more accurately aligning the scans to fix the ARs of interest within the entire time sequence. Despite this, we do observe oscillations also seen Figure 4 (redshift/blueshift PFD variance and skewness plots). These oscillations, associated with the AR regions exhibiting solar eruptions, occur with a period of ~ 10 minutes and may be related to photospheric p-mode acoustic waves.

Advancing our alignment method is expected to reduce noise in our PFD properties and reveal additional physical information contained at the sub-pixel level and provide improved physical constraints on observed quantities. We also intend to gather additional data, from other solar observatories/instruments, such as the New Solar Telescope (NST). Additional data from various solar telescopes will provide insight on the effects of higher resolution pixel statistics. Also, obtaining GOES X-ray will provide us a reliable means of determining when flare initiation occurs for each of these flare events, information that will help determine changes in PFDs that may be connected to solar eruptions.

5. Summary

We have developed a new method to analyze high-resolution spectral data of the solar photosphere. The data format is a 2-D time-series of images in which each pixel contains the intensity and polarization (Stokes parameters) spectra in the wavelength regime of interest. The method can be used for emission or absorption lines. The spectral data in each pixel are analyzed to compute the line intensity peaks/dips, position of the lines, line width, asymmetry, and flatness of the tail. Changes in these spectral properties contain extractable information concerning changes in the sub-grid plasma and magnetic field dynamics. The pixel fluctuations $\delta\mathcal{X}$ in spectral quantities $\mathcal{X}$—for example, the line center, asymmetry, and flatness of the line profile—are statistically analyzed using pixel distribution functions (PFDs) $P(\delta\mathcal{X}_m)$, where $\delta\mathcal{X}_m(n)$ is the fluctuation in the quantity $\mathcal{X}$ in the n-th pixel of the m-th image, and $P(\delta\mathcal{X}_m)$ is the histogram of the number of pixels with fluctuation value of $\delta\mathcal{X}$. Incrementing the image frame counter m is equivalent to advancing time. The statistical properties of the PFDs such as variance, skewness, and kurtosis are computed as functions of time (m), and the temporal variations in these quantities can be precisely quantified. This method is suited for analyzing large volumes of high-resolution (spatial, temporal and spectral) 2-D time-series data. It is applicable to remote-sensing photon data from the photosphere and chromosphere where regions of interest in a "surface" (i.e., a thin layer) can be defined.

REFERENCES

Babcock, H. W., Astrophys. J., **133**, 572 (1961).

Balasubramaniam, K. S., and Pevtsov, A. A., Proc. SPIE **8148**, 814809, doi:10.1117/12.892824 (2011).

Carrington, R. C., Mon. Not. R. Astron. Soc., **20**, 13 (1860).

Chen, J., Space Sci. Rev. **95**, 165 (2001).

Cheung, M. C. M., Rempel, M. Title, A. M., and Schüssler, M., Astrophys. J., **720**, 233 (2010).

Domingo, V., et al., Sol. Phys., **162**, 1 (1995).

Hale, G. E., Astrophys. J., **28**, 315 (1908).

Hodgson, R., Mon. Not. R. Astron. Soc., **20**, 16 (1860).

Pietarila Graham, J., Danilovic, S., and Schüssler, J., Astrophys. J., **693**, 1728 (2009).

Scherrer, P. H., Bogart, R. S., Bush, R. I., Hoeksema, J. T., Kosovichev, A. G., and Schou, J., Sol. Phys., **162**, 129 (1995).

Schuck, P. W., Chen, J., Schwartz, I. B., and Yurchyshyn, V. Astrophys. J., **610**, L133 (2004).

Stein, R. F. and Nordlund, A., Astrophys. J. Lett., **753**, L13 (2012)

Strous, L. H., Scharmer, G., Tarbell, T. D., Title, A. M., and Zwaan, C., Astron. Astrophys., **306**, 947 (1996).

Strous, L. H., and Zwaan, C., Astrophys. J., **527**, 435 (1999).

Zirin, H., *Astrophysics of the Sun*, Cambridge University Press, Cambridge, UK (1988).

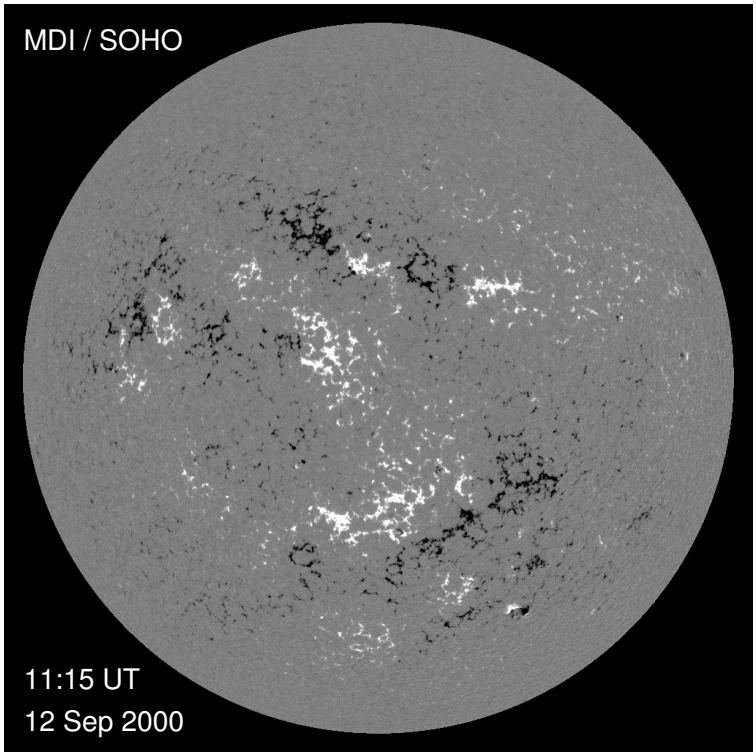

Fig. 1.— Magnetograph image obtained by the Michelson Doppler Imager (MDI) on board SOHO. The white (dark) patches show magnetic fields pointing out of (into) the Sun along the line of sight (LOS).

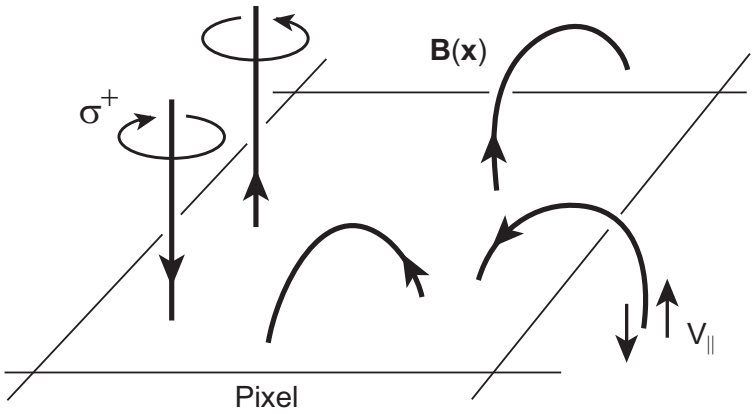

Fig. 2.— Schematic of sub-grid magnetic field and cancellation of Zeeman-induced polarization.

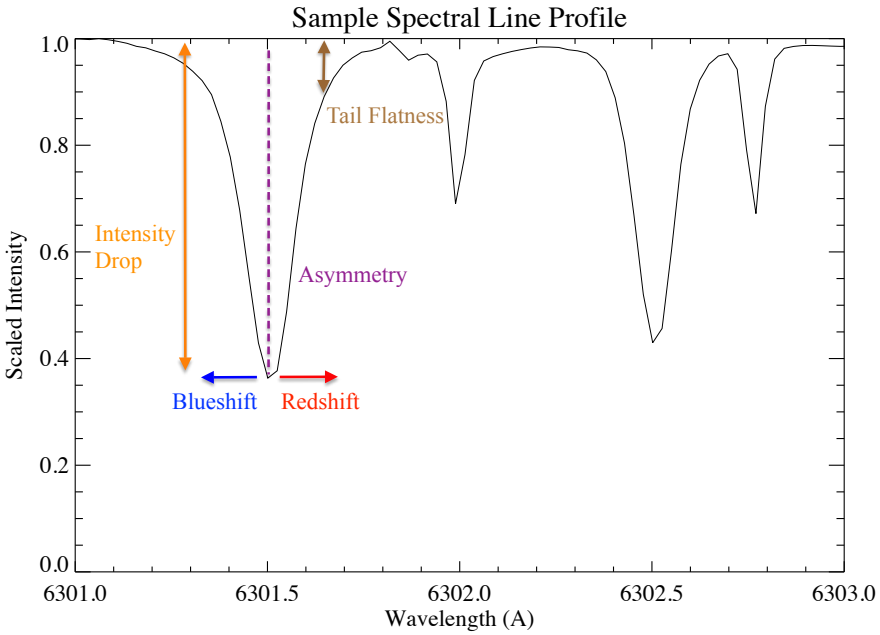

Fig. 3.— A spectral line intensity profile. A Stokes I (total spectral intensity) area scan data obtained by the SOLIS VSM instrument. The wavelength range shows two photospheric absorption lines, Fe I 6301.5 Å and Fe I 6302.5 Å), and two smaller telluric (atmospheric) lines. The VSM spectral resolution is $\Delta\lambda \simeq 0.024\mathring{A}$ with $1''$ (arcsecond) spatial resolution.

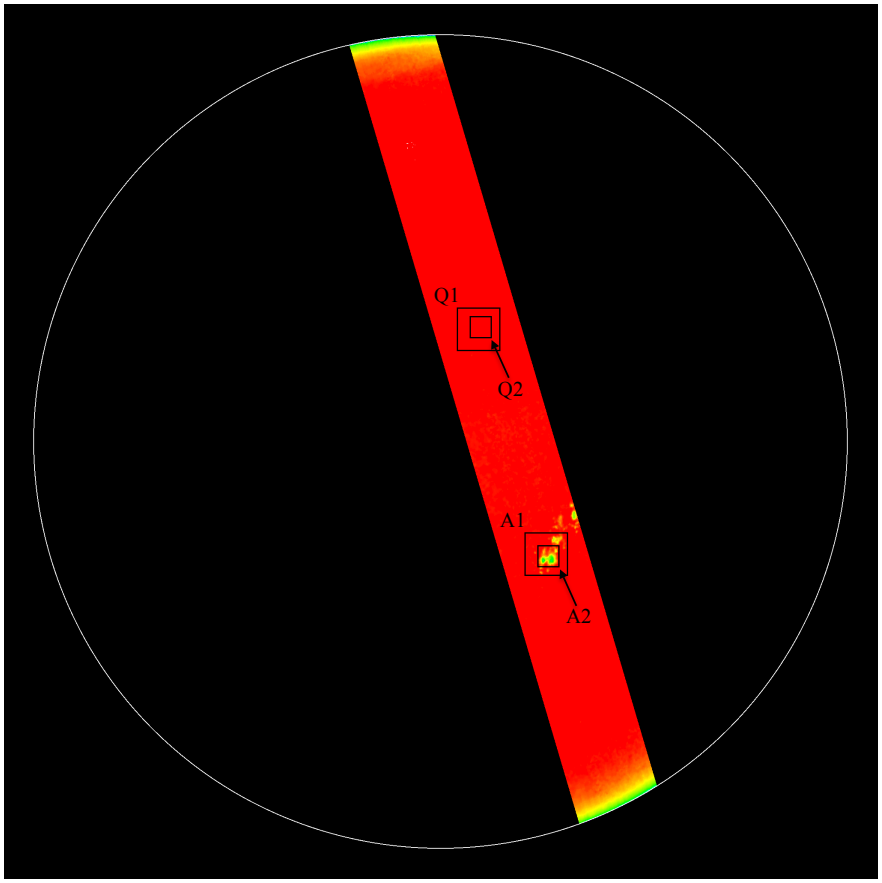

Fig. 4.— A spectral intensity (Stokes I) area scan aligned with the solar disk (outline in white). The four boxes represent groups of pixels analyzed separately. They correspond to 100×100 and 50×50 boxes containing a solar active region ($A1$ and $A2$, respectively) and 100×100 and 50×50 boxes in a quiet-Sun region ($Q1$ and $Q2$, respectively). Over time, the four pixel regions shift to the right with the rotating solar surface. Red: high intensity. Green: low intensity.

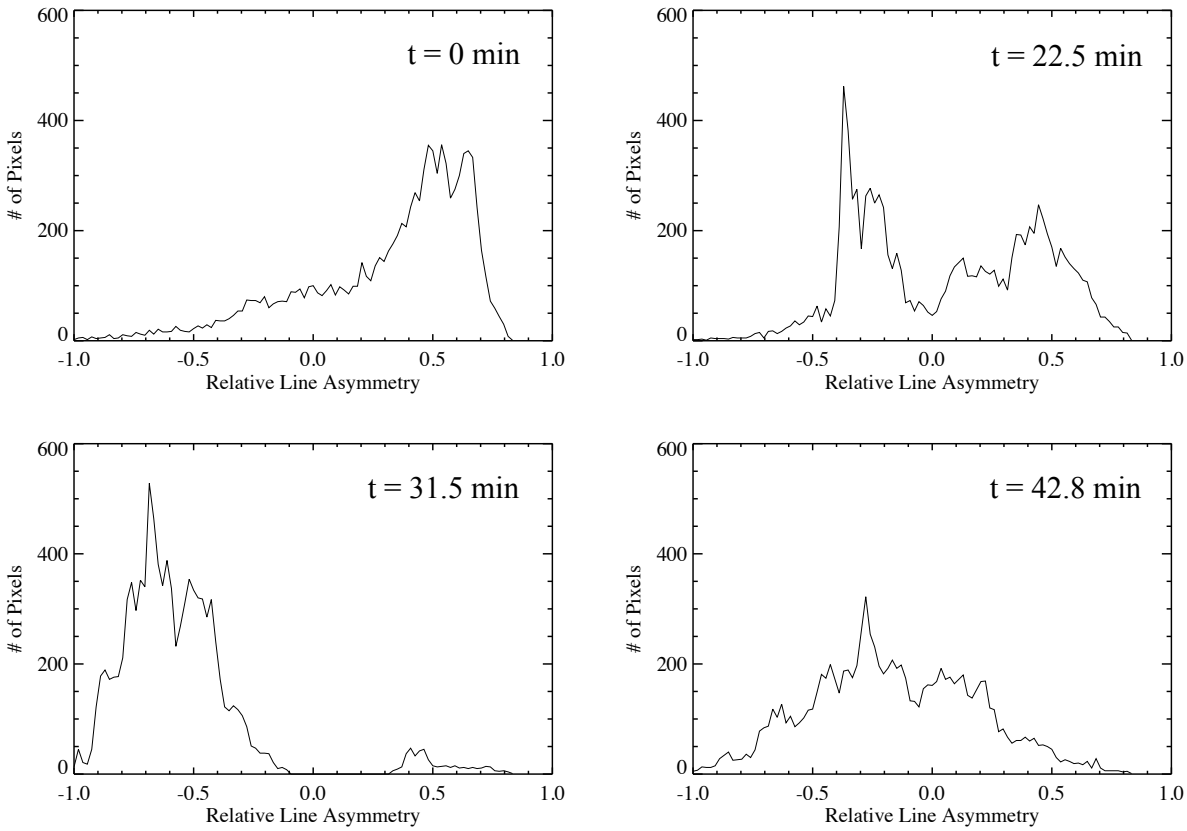

Fig. 5.— An example of a time-evolving PFD for absorption line (Fe I 6301 Å) asymmetry. The time-evolving statistical measures of the PFDs are used to characterize and quantify quiet-Sun and active regions in this report.

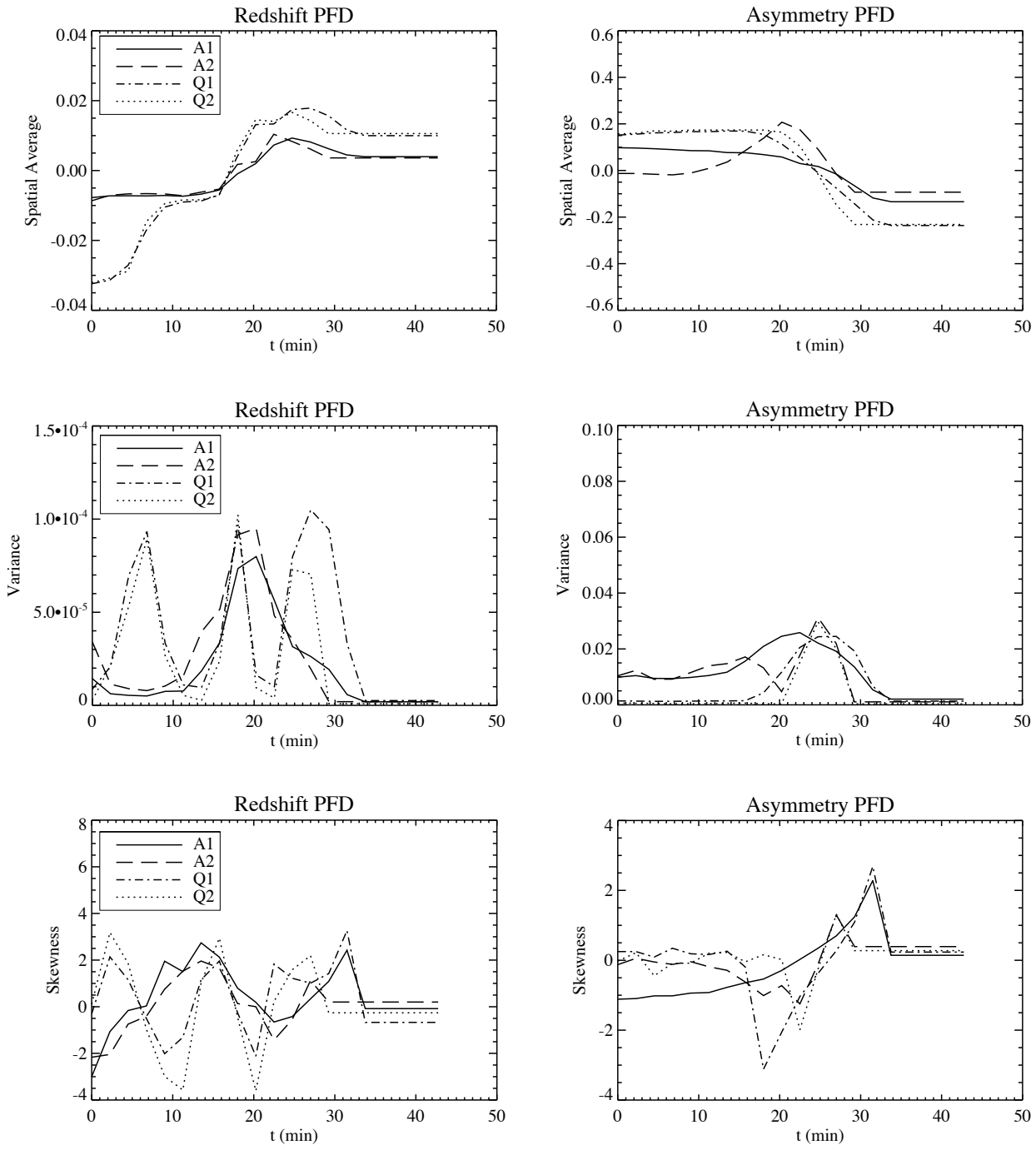

Fig. 6.— Comparisons of statistical profiles of the collective Fe I 6301.5 Å absorption line redshift and asymmetry for each box of pixels shown in Figure 4. From the time-varying PFD statistics, quiet-Sun ($Q1/Q2$) regions and active ($A1/A2$) regions appear to be more characterized by statistical differences in their photospheric absorption line redshift and asymmetry properties.

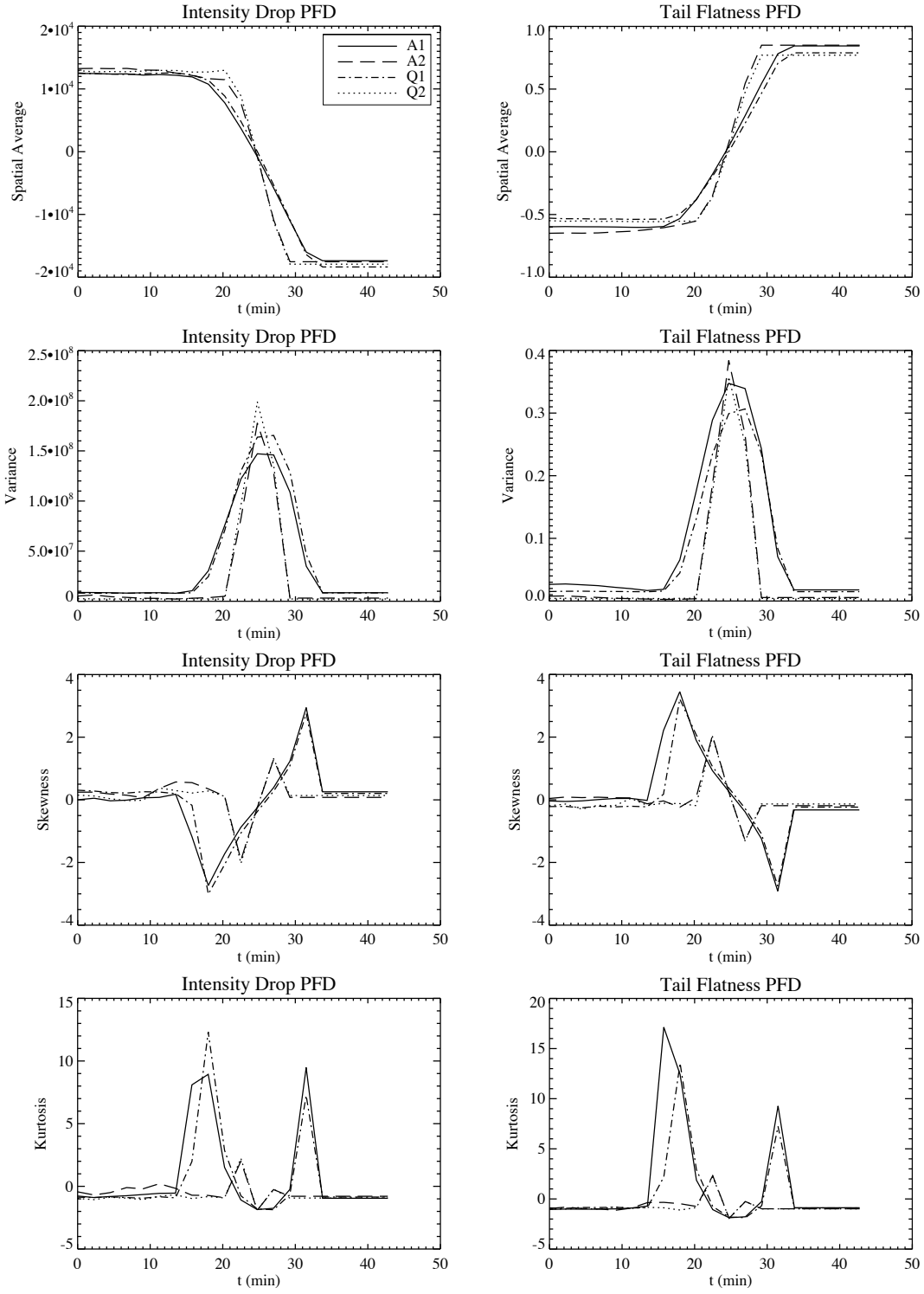

Fig. 7.— Statistical profiles of the collective Fe I 6301.5 Å absorption line intensity drop and tail flatness for the pixel boxes in Figure 4. Unlike in Figure 6, pixel sample size appears to be characterized by statistical differences in absorption line intensity drop and tail flatness.

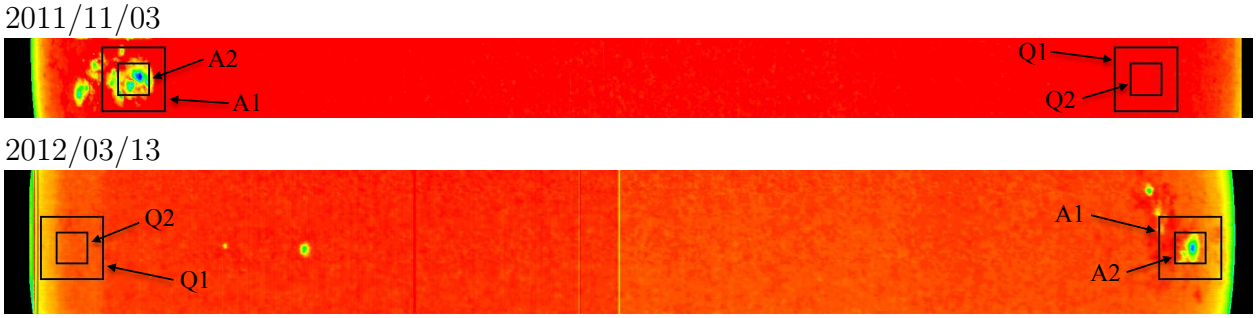

Fig. 8.— Analyzed spectral intensity area scans ($t = 0$ s) corresponding to flare events on Nov. 3, 2011 (top) and Mar. 13, 2012 (bottom). Like in Figure 4, the four boxes represent groups of AR and control (quiet-Sun) pixels analyzed separately. The ARs and boxes are in fixed locations for each time series.

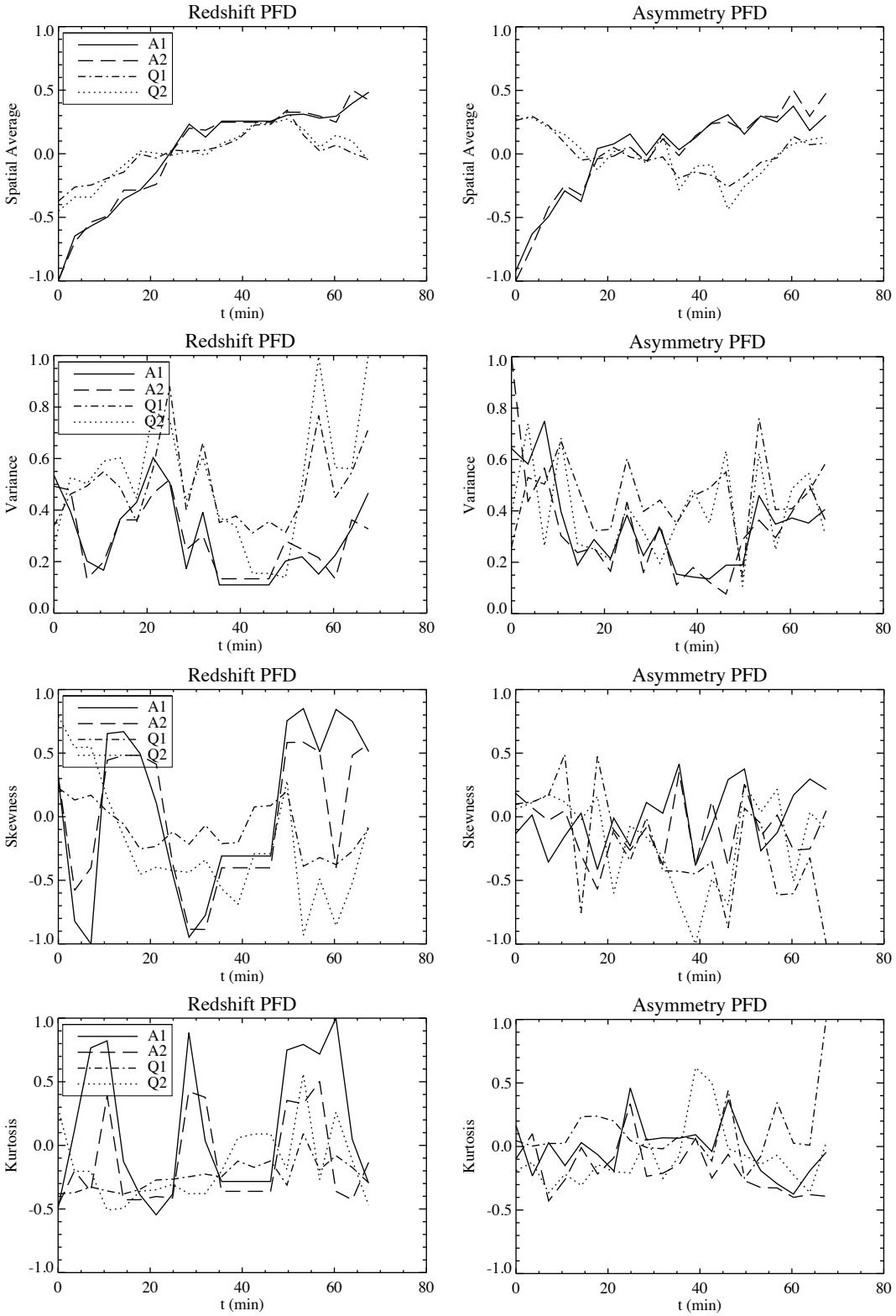

Fig. 9.— Statistical profiles of the collective Fe I 6301.5 Å absorption line redshift and asymmetry for the pixel boxes in Figure 8 (top). All statistical properties are plotted relatively.

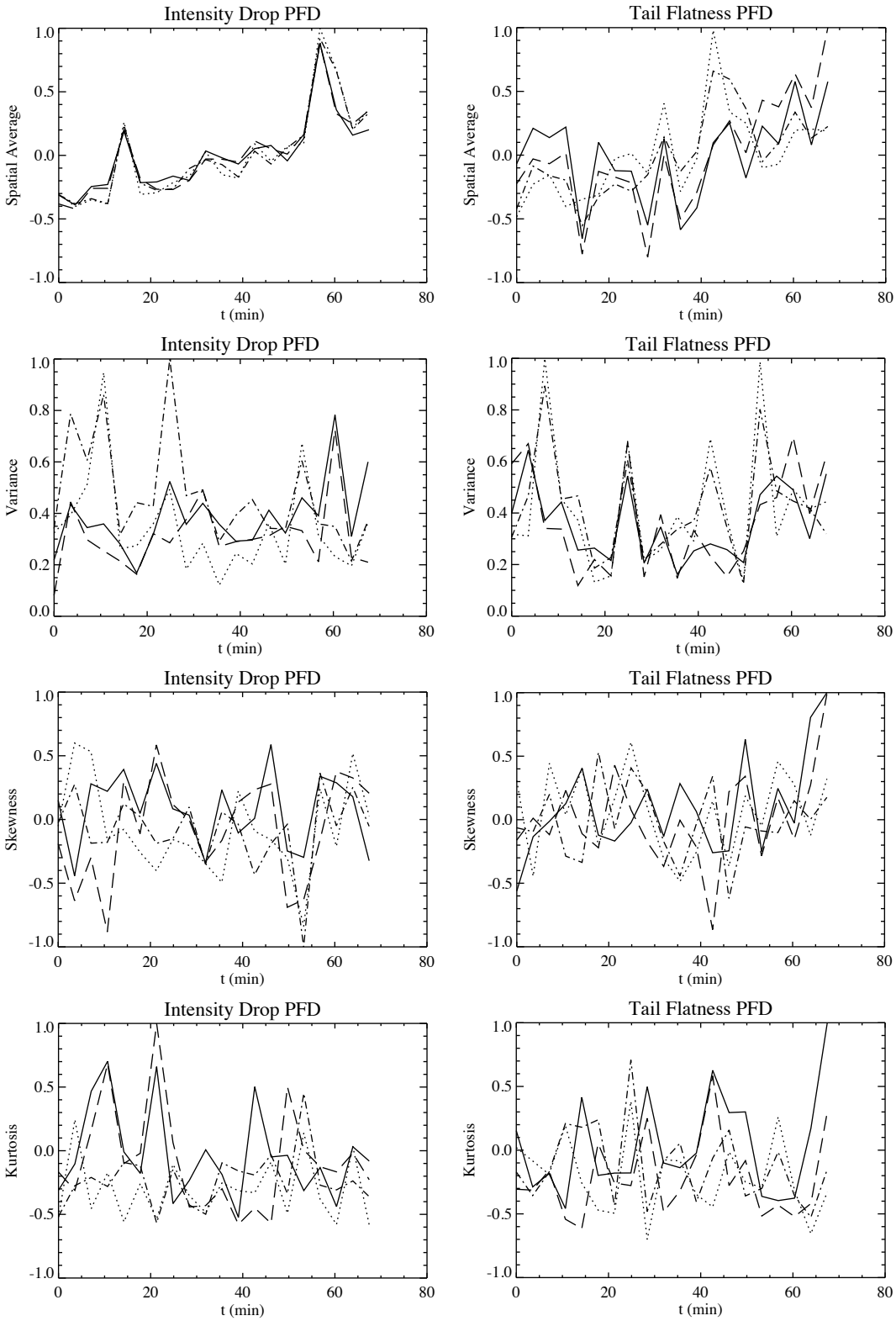

Fig. 10.— Statistical profiles of the collective Fe I 6301.5 Å absorption line intensity drop and tail flatness for the pixel boxes in Figure 8 (top). All statistical properties are plotted relatively.

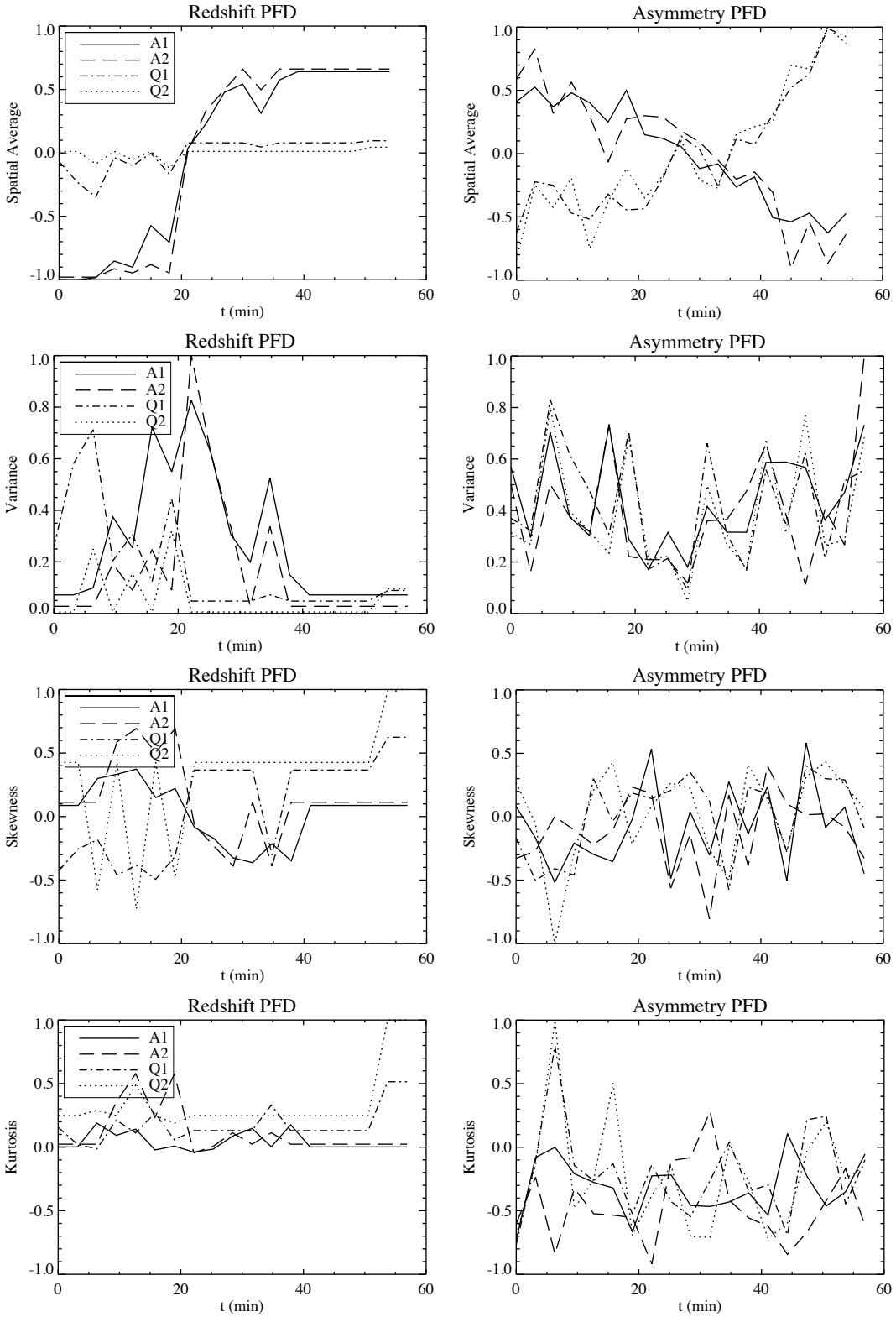

Fig. 11.— Statistical profiles of the collective Fe I 6301.5 Å absorption line redshift and asymmetry for the pixel boxes in Figure 8 (bottom). All statistical properties are plotted relatively.

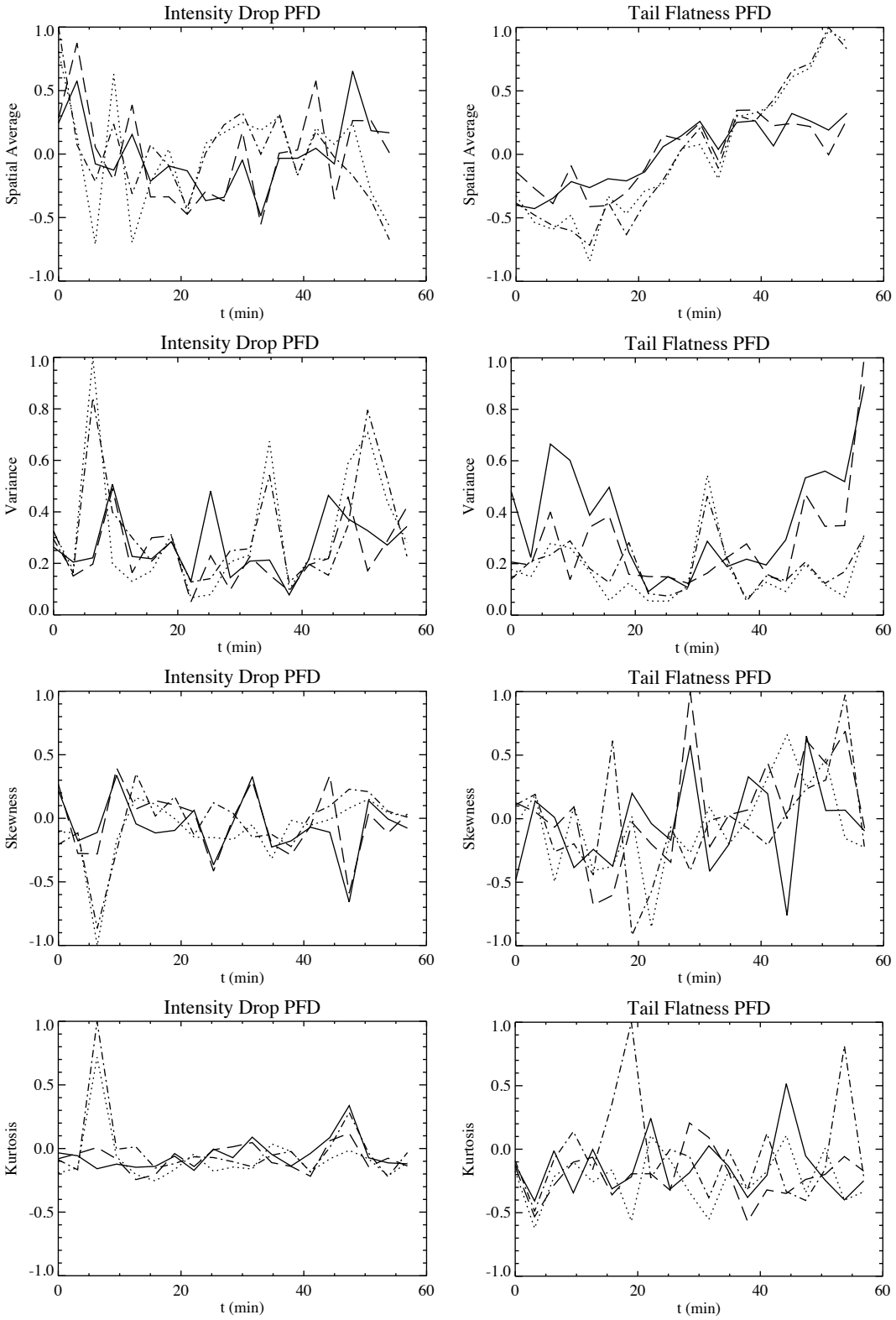

Fig. 12.— Statistical profiles of the collective Fe I 6301.5 Å absorption line intensity drop and tail flatness for the pixel boxes in Figure8 (bottom). All statistical properties are plotted relatively.